

Earthquake-induced landslides monitoring and survey by means of InSAR

Tayeb SMAIL¹, Mohamed ABED¹, Ahmed MEBARKI^{2,3}, Milan Lazecky^{4,5}

¹Department of Civil Engineering, Saad Dahlab University, Blida City, Algeria

²[Univ Gustave Eiffel, Univ Paris Est Creteil, CNRS, UMR 8208, MSME, 5 Bd Descartes, F-77454 Marne-la-Vallée, France](#)
~~University Gustave Eiffel, Laboratory Multi Scale Modeling and Simulation (UMR 8208 CNRS/UPEC/U.Eiffel), 5 Bd Descartes, 77454, Marne-La-Vallee, France~~

³Nanjing Tech University, 5 New Mofan Rd, Gulou, Nanjing, Jiangsu, Chine - Permanent Guest Professor within “High-Level Foreign Talents Programme” grant

⁴IT4Innovations, VSB-TU Ostrava, 17, Listopadu 15, 70833 Ostrava-Poruba, Czech Republic

⁵School of Earth and Environment, University of Leeds, Leeds LS2 9JT, UK

Correspondence to: SMAIL Tayeb (st_gc@hotmail.fr)

Abstract. This study uses interferometric SAR techniques to identify ~~and track earthquake-induced landslides~~ ~~landslides and as well as~~ lands prone to landslides, ~~by detecting deformations fringes and changes~~ in areas struck by earthquakes. The pilot study ~~area~~ investigates the Mila region (~~in Algeria~~) which suffered significant landslides and structural damages (earthquake: Mw-5, 2020-08-07): ~~the study checks ground deformations and tracks earthquake induced landslides.~~ DInSAR analysis ~~shows~~ normal interferograms, with ~~atmospheric contribution, and slight~~ small fringes. ~~However, i~~ The Coherence Change Detection (CCD) and DInSAR analysis were able to identify many landslides and ground deformations confirmed also ~~by~~ In addition, SAR images and Sentinel-2 optical images ~~(Sentinel-2) confirm and site field inspection.~~ The most important displacement (2.5 m), located in Kherba neighborhood, caused ~~causing~~ severe damages to dwellings. It is worth notice that CCD and DInSAR are very useful since they were also able to identify ground cracks surrounding a large zone (3.94 Km² area) in Grarem City whereas the Sentinel-2 optical images could not detect them. ~~These unnoticed ground disorders were confirmed during fields inspection. Such results have key importance since they can serve as an alert to monitor the zone at the proper time.~~ Although, ~~Displacement displacement time-time~~ series analysis of ~~224 many~~ interferograms ~~(April 04-2015 to September 09-2020) using LiCSBAS~~ were performed using LiCSBAS ~~did not detect any pre-event~~ geotechnical precursors, the post-event analysis shows a 110 mm/y subsidence velocity in the ~~back-back~~ hillside of Kherba, ~~and high displacement velocity at specific points in Grarem region.~~

1 Introduction

Although it is still challenging to predict exactly where and when natural hazards (earthquakes, landslides, floods, etc.) might occur, the capacity to monitor and survey the zones prone to important landslides as well as the capacity to identify and locate those impacted by earthquakes are key issues in risks mitigation, reduction, preparedness and adaptation. Actually, since earthquakes and landslides might occur in many places worldwide, they might cause a huge number of victims, important socio-economic, assets damages and losses. Their impact can be significantly reduced thanks to satellite imaging which allows prediction and early alerts of some landslide cases (Del and Idrogeologico, 2012; Jacquemart and Tiampo, 2021; Moretto et al., 2021).

36 It is then worth detecting or predicting critical ground changes at specific places, either after a geotechnical ~~disorder-hazard~~
37 occurs due to landslides and earthquakes mainly, or before it is suddenly triggered (Bakon et al., 2014; Galve et al., 2015).
38 Such challenges can be tackled by regular image processing oriented landslides areas monitoring, in the aftermath of
39 earthquakes, ~~by means of using~~ SAR interferometric methods and optical images, for instance. Actually, since ~~InSAR~~
40 (~~Interferometric~~-Synthetic Aperture Radar) is an active sensor system that uses microwave signals to collect data backscattered
41 from the earth's surface, the use of satellite imaging systems ~~like Interferometric InSAR methods~~ appears as a cost-effective
42 way for measuring millimeter-level displacements of the earth surface (Herrera et al., 2009), at a regional scale and can be
43 used as an early warning system for the safety of structures and their surroundings (Galve et al., 2015; Roque et al., 2015).

44 The expected outcomes are based upon the processing of SAR data ~~making use as it uses of~~ Differential InSAR (DInSAR),
45 Coherence Change Detection (CCD), and time series analysis (~~using LiCSBAS software~~). ~~LiCSBAS of that exploit/exploits~~
46 ~~the LiCSAR data which is a system for and that process processing InSAR datasets automatically automatically (Sentinel-1~~
47 ~~dataset) using LiCSBAS software, to illustrate the taking~~ advantages of high-resolution SAR sensing, ~~in order to track for the~~
48 ~~objective of tracking~~ ground changes and landslides.

49 The ~~performed~~ SAR analyses ~~can reveal some aim to detect~~ ground ~~deformations changes detected~~ through DInSAR and
50 CCD ~~maps investigations~~, as they consider, for illustrative purposes, a city in Algeria struck by an earthquake ~~as it is shown~~
51 ~~the illustrative purposes for the 7th of August 2020 earthquake (August 7, 2020: Algeria, Mila):~~ ~~The the ground se~~
52 ~~deformations and displacements displacements, which occurred in Kherba City the and northeastern part at the~~ Grarem City
53 ~~(northeastern part of Mila downtown, (2 km from Mila downtown) and Kherba City are investigated presented as,~~ caused a
54 ~~loss of coherence in CCD maps and as fringes in DInSAR maps. Their extend affects affected areas of around span over~~
55 3.94 km² for Grarem and 2.1 km² for the Kherba landslides ~~area case~~. Furthermore, ~~the a~~ time-series analysis ~~of LiCSAR data~~
56 ~~performed out by using LiCSBAS software, investigates reveals a slow~~ possible existence of precursors in geotechnical
57 ~~conditions subsidence deformation signal in the left part of the other of Kherba landslide side area in the Kherba case.~~

58 The ~~formed fringes and coherence loss in the~~ Grarem case indicate the boundary of a potential land failure. The results can
59 ~~serve as early warning information provided by the InSAR monitoring system, since the area should be monitored to investigate~~
60 ~~the existent of plane failure or probable growing slope failures disorder.~~

61 2 Land and ground movements monitoring and surveying in the aftermath of an earthquake

62 2.1 Satellite images and methods - Case study

63 The present research study is multifold. It aims to use InSAR image processing for various purposes, in the case of landslides
64 and earthquakes:

- 65 - Use the InSAR in the aftermath of an earthquake in order to identify the geotechnical ~~disorders hazards displacements~~
66 ~~or deformations~~, their extent, and locations. The Differential radar interferometry and the Coherence Changes
67 Detection are the most adapted methods for ground and soil surfaces changes detection (Jung and Yun, 2020; Meng
68 et al., 2020; Pawluszek-Filipiak and Borkowski, 2020; Tampuu et al., 2020; Tzouvaras et al., 2020). A city, Mila, in
69 Northern Algeria, is considered as the pilot study. It has been struck by an earthquake in August 2020. The ~~geotechnical~~
70 ~~hazards disorders~~ (landslides and surface ~~faults~~) ~~cracks~~ have ~~been~~ affected significantly, during the ~~same~~ earthquake
71 events series, two distinct zones being distant by almost 15 km from each other (~~Kherba and Grarem~~).
- 72 - Use ~~the time series~~ analysis to ~~investigate study the mean~~ displacements and ~~mean displacement their~~ velocity
73 ~~velocities~~ before and after the occurrence of the main shock. For the city of Mila, the time series is performed out for
74 a period extending from April 2015 up to October 2020, i.e. a long period before ~~the (April 2015 up to March 2020,~~
75 ~~i.e. 5 entire years)~~ ~~and a period 4 months ahead of~~ the main shock in order to avoid a disturbance or bias that might
76 be related to seasonal effects such as rains and vegetation effects (~~Lazecyk et al., 2020a~~); (~~Lazecyk et al., 2020a~~), and

a short period (4 months) ahead of the event date in order to check investigate the historical development of the landslide.

- Compare and correlate the InSAR images processing results with the satellite optical images observations.

2.2 Pilot zone, earthquakes and landslides - Observed disorders

The case study area lies in Mila Province which is located in the northeast part of Algeria (Mediterranean zone), near the Dam of Beni Haroun. The Mediterranean zone is seismically active because of the northward convergence (4-10 mm/yr) of the African plate relative to the Eurasian plate along a complex plate boundary (Frizon de Lamotte et al., 2000; Mouloud and Badreddine, 2017; Peláez Montilla et al., 2003; USGS, n.d.). Throughout the last years, several landslide events have taken place in the wider region of Mila (Merghadi et al., 2018). Merghadi et al. (2018) constructed a detailed landslide inventory map of the study area. The seismic activities and landslides pose a persistent threat for built-up areas and facilities, such as roadways, bridges and tunnels, which need continuous monitoring and survey.

After an earthquake (Mw 5, 2020-08-07, epicenter 36.550° N - 6.271° E, Depth=10 km, (USGS)) that struck this region, important landslides were mostly observed in Mila City and its surroundings, see Figs. 1 and 2-3. Although, the earthquake was moderate, Beni Haroun Dam and the two large bridges built on the RN 27 highway needs to be inspected and their possible displacements monitored.

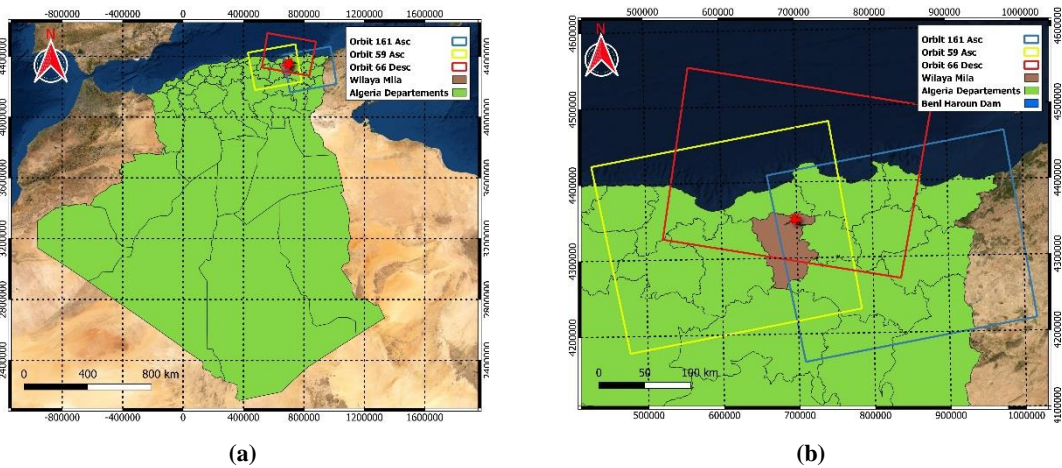
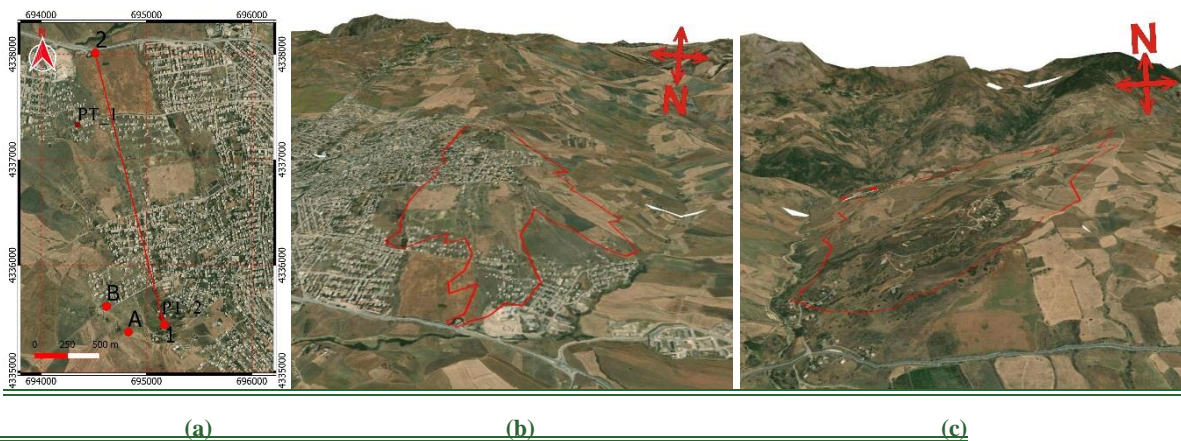


Figure 1. Mila location map (a), ascending and descending orbits footprints. Red stars indicate earthquake epicenter (QGIS, ESRI basemap).

In the present, two areas are studied, i.e. Kherba and Grarem Cities. The altitude at the top point 1 (Fig. 42.a) in Kherba hill is 654 m and in 411 m for the upper point (2) is 411 m a.s.l. in the upper point (2), located at with a horizontal length between 2.14 km distance with 11.34% and a slope of 11.34%. The maximum ground horizontal offset reached 2.5 m and the vertical deformations exceed 1.8 m (Fig. 23.b) at the top of Kherba hill (point A Fig. 42.a). The slope failure boundary of Kherba City is mapped as shown in Fig. 42.b. The Grarem area of interest (AoI) is located at east north of Mila in a hilly ground with an average slope reaching 12.5%, see Fig. 42.c.



103 **Figure 42.** 3D view of AoIs, Kherba AoI and Grarem using QGIS with DEM SRTM 1sec and ESRI basemap, a & b are Kherba AoI, c is
 104 the Grarem case area, the red polygon is the boundary of change detected by InSAR.



106
 107
 108 **Figure 23.** Ground cracks due to landslides in Kherba, Mila, ~2.5m offset towards the North, a. Drone aerial photo from (LNHC), b. & c.-
 109 Lateral displacements (Photos: courtesy M. Yacoub A., University of Setif, Algeria).

110 **2.3 Pilot zone - Data and images collection**

111 The dataset used for this study is collected from European Space Agency (ESA), via the Copernicus Open Access portal, and
 112 from the Alaska Satellite Facility (ASF DAAC). The C-band Sentinel-1 A and B, launched in 2014 and 2016 respectively,
 113 provide regular data-sets. ~~The Sentinel-1 sensors have a wavelength of 5.546 cm (ESA), suitable for change detection and~~
 114 ~~monitoring of large areas, and are right side-looking with an incidence angle ranging approximately from 20° to 46° (ESA,~~
 115 ~~2012), which are suitable for change detection and the monitoring of large areas. (Morishita, 2021).~~ For the InSAR use, the
 116 Interferometric Wide (IW) swath Single Look Complex (SLC) data is selected and processed with the open-source software
 117 SNAP (Sentinel Applications Platform). It is worth using data from many orbits to monitor the AoIs due to different oriented
 118 directions, incidence angles of satellites, and the ground topography. The optical images of Sentinel-2 ~~sensors-satellites~~ are
 119 obtained from ESA, whereas downloading and processing data is done via QGIS, Semi-Automatic Classification Plugin (SCP)
 120 (Congedo, 2021).

121 For Mila region, the AoI is covered by 3 orbits ~~two are~~ ascending (66, 59) and ~~one is~~ descending ~~66, 59, and~~ 161
 122 (Fig. 1). Since the present study intends to detect the areas influenced by landslides, many pre-event and post-event data
 123 ~~are were~~ used ~~in order to get an accurate evaluation of the event.~~ Eighteen Sentinel-1 A and 17 Sentinel-1 B ~~images (a total of~~
 124 ~~35) images were~~ downloaded ~~to monitor Mila's area~~ for the period ~~of from~~ 1 July 2020 to 26 October 2020, ~~to monitor Mila's~~
 125 ~~area, and are being used to perform out a detailed study on the land deformations and the dynamics of the landslide.~~ Table 1
 126 summarizes the appropriate interferograms, ~~i.e. those having with that have~~ a small perpendicular baselines and short temporal
 127 baselines. Tables 1, 2, and 2bis ~~presents all the images, their used in this study and they are labelled as labels as IFG-ID,~~
 128 ~~Orbits, and dates of their acquisitions summarize the whole data collected for the case study.~~

129 **Table 1.** Characteristics of Sentinel-1 InSAR pairs ~~for Mila case used for this study.~~

IFG-ID	Track	M Date	S- Date	Bp [m]	Bt [days]
IFG- 10		2020-07-22	2020-07-28	-9.99	6
IFG-1		2020-07-28	2020-08-03	40.90	6
IFG-2	66 ASCENDING	2020-07-28	2020-08-03	40.62	6
IFG-3		2020-08-03	2020-08-09	-51.47	6
IFG-4		2020-08-03	2020-08-09	-50.76	6
IFG-5		2020-08-09	2020-08-15	-27.57	6

IFG-6		2020-08-09	2020-08-15	27.62	6
IFG-7		2020-08-15	2020-08-21	-16.19	6
IFG-8		2020-08-21	2020-08-27	42.43	6
IFG-9		2020-08-27	2020-09-02	-28.59	6
IFG-10		2020-09-02	2020-09-08	29.26	6
IFG-11		2020-09-08	2020-09-14	17.95	6
IFG-12		2020-09-14	2020-09-20	-6.05	6
IFG-13		2020-09-20	2020-10-02	-4.64	12
IFG-14		2020-10-02	2020-10-14	18.13	12
IFG-15		2020-10-14	2020-10-26	-49.36	12
<hr/>					
IFG-16		2020-07-27	2020-08-02	69.64	6
IFG-17		2020-08-02	2020-08-08	-75.10	6
IFG-18	59 ASCENDING	2020-08-08	2020-08-14	-8.86	6
IFG-19		2020-08-14	2020-08-20	175.97	6
IFG-20		2020-08-20	2020-08-26	-226.75	6
<hr/>					
IFG-21		2020-07-22	2020-07-28	-169.19	6
IFG-22		2020-07-28	2020-08-09	30.39	12
IFG-23		2020-07-28	2020-08-03	99.88	6
IFG-24	161 DESCENDING	2020-08-03	2020-08-09	-70.12	6
IFG-25		2020-08-09	2020-08-15	2.14	6
IFG-26		2020-08-15	2020-08-21	121.22	6
IFG-27		2020-08-21	2020-08-27	-196.82	6

130 **Bt:** temporal baseline; **Bp:** perpendicular baseline.

131 The All-temporal baselines time interval for all InSAR pairs processing is are 6 days, except the last three pairs of the 66
132 ascending pass-orbit 66 that have 12 days. Furthermore, since a bad coherence map of the IFG-24 (Orbit 161), may lead to
133 misinterpretation of results, early-prior acquisition images data (before the 3rd of August) with a time interval of 12 days are is
134 selected for to generate the co-event interferogram for the 161-descending pass (IFG-22). Therefore the temporal baseline is
135 12 days. The gray cells-rows in Table 1 represent the co-event interferograms of the three orbits. The perpendicular baselines
136 guarantees also a good quality of InSAR studies (Braun, 2019). As LiCSBAS time series analysis aims to investigate long
137 period displacements and velocities over a large area, 34 interferograms IFGs from the from orbit 66 and 190-interferograms
138 interferograms collected IFGs for from the 161 ascending track (Table 2), are selected for the present study.

139 **Table 2.** LiCSAR frames, analyzing periods and the total number of IFGs used in this study.

Frame ID	Date		Period	IFGs
	Start	End		
161A_05343_090806	2015-4-26	2020-9-26	66 month	190
066D_05394_131311	2020-4-5	2020-9-26	6 months	34

140 **Table 2bis.** Sentinel-2 optical images collected for the study case.

Frame ID	Date	Duration days, to the main shock
Image 1	2020-07-30	-7 days
Image 2	2020-08-09	+ 2 days

141 3 Methodology description and results

142 Four aspects are investigated and compared in the present case study:

- 143 - The SAR Interferometric (InSAR) methodology, which is subdivided into three sub-groups:
 - 144 - DInSAR for the phase changes (fringes),
 - 145 - CDD for the coherence change detection,
 - 146 - Time series analysis and LiCSAR data.
- 147 - The optical image processing.

148 ~~For the results section, every image contains the description of its source, by i.e. IFG-ID (Tables 1, 2, and 2bis) or by the~~
149 ~~image's acquisitions dates.~~

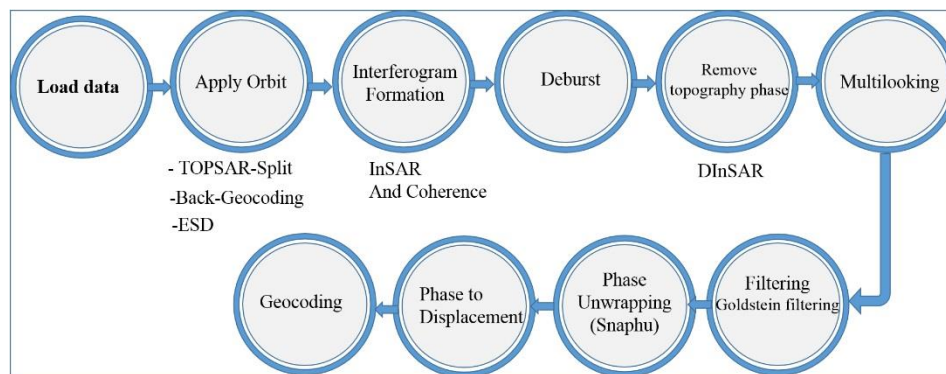
150 3.1 SAR Interferometric methodology

151 The ~~Interferometric~~ Synthetic Aperture Radar (~~In~~SAR) is an active microwave imaging system. It is independent of sunlight
152 and ~~can~~ penetrates clouds, unlike ~~optical imaging systems which are passive~~ passive optical imaging systems. ~~The~~
153 ~~interferometric InSAR method~~ uses the phase components of co-registered SAR images of the same pixel to estimate the
154 topography and to measure the surface change in the target area (Kim, 2013). At least two constellation images are needed to
155 generate an interferogram, which contains topographic, atmospheric effect, baseline error, and noise components (Goudarzi,
156 2010; Kim, 2013; Netzband et al., 2007):

$$157 \phi = \phi_{disp} + \phi_{flat} + \phi_{topo} + \phi_{atm} + \phi_{orbit} + \phi_{noise} \quad (1)$$

158 Where ϕ_{disp} is the line-of-sight (LOS) displacement, - ϕ_{flat} the flat earth phase, - ϕ_{topo} the topographic phase, ϕ_{atm} is an
159 atmospheric phase, ϕ_{orbit} , the baseline phase and ϕ_{noise} is noise phase contribution (Kim, 2013).

160 The main steps ~~for the study of processing, by data~~ using SNAP software (DInSAR and CCD), are depicted in Fig. 34. It's
161 worth notice that for CCD processing, it is not necessary to follow the whole (DInSAR, Phase Unwrapping, and Phase to
162 displacement).



163
164 **Figure 34.** Workflow chart for the DInSAR processing using (SNAP) software.

165 3.1.1 Differential radar interferometry (DInSAR)

166 Differential radar interferometry (DInSAR) exploits the phase difference to measure coherent changes or deformation between
167 two image acquisitions. It is often used for ground subsidence measurement (Canaslan Çomut et al., 2020; Galve et al., 2015).
168 One of DInSAR's limitations is that the changes are not measurable in the case of non-coherent events (e.g., rapid landslide)
169 (Braun, 2019) ~~which such as is the case in this present study.~~

170 3.1.2 Coherence Change Detection (CCD) ~~Times series analyses~~

171 The estimated coherence is considered as a quality indicator of an interferogram (Jacquemart and Tiampo, 2021). Actually, it
172 indicates that the phase and amplitude of the received signal express the degree of similarity between the images pair. The
173 pixel coherence γ of two SAR images is estimated on the basis of N neighboring pixels (Jia et al., 2019; Wang et al., 2018).

$$174 \gamma = \frac{\sum_{i=1}^N S_{1i} S_{2i}^*}{\sqrt{\sum_{i=1}^N |S_{1i}|^2 \sum_{i=1}^N |S_{2i}|^2}} \quad (2)$$

175 Where: S_{1i}, S_{2i} , are the complex signal values of the SAR image pair, N is the window of neighboring pixels, * is the complex
176 conjugate.

177 The coherence values range between 0 and 1 so that the map is represented as a gray color which 0 is white and 1 is black.

178 3.1.3 Time series analysis and LiCSAR data

179 The “Looking into Continents from Space with Synthetic Aperture Radar” (LiCSAR) LiCSAR-system processes automatically
180 Sentinel-1 InSAR-datasets for InSAR use, and generates wrapped, unwrapped interferograms and coherence maps (Lazecký
181 et al., 2020b), with a final product resolution of ~26.5 m (Lazecký et al., 2020a). For such purposes, the open-source LiCSBAS
182 software, adopted in the present study, is used for InSAR time series analysis based on LiCSAR data. It is able to can generate
183 maps of mean-LOS displacement velocity displacement and deformation time series for all processed frames. Furthermore, it
184 is easy to implement and does not request high-performance computing facilities (Morishita, 2021).

185 In addition, the mechanism of landslides can be thoroughly studied through LiCSBAS analyses. They rely on the the
186 InSAR time-series analysis package integrated with Looking into Continents from Space with Synthetic Aperture Radar
187 (LiCSAR), (Lazecký et al., 2020b). Such time-time-series analyses are very helpful-useful in identifying, for a given landslide
188 or geological-ground disorder deformations and displacements, the prior patterns of ground movements versus the time as well
189 as foreseeing a potential disorder hazards.

190 3.2 Optical image processing

191 The optical methods-sensors are a-passive detection methodsmeans way-that needs sunlight and clear weather conditions in
192 order-to exploit the data. The Sentinel-2 is a multi-spectral instrument (MSI) that measures reflected solar radiance in 13 bands
193 with a spatial moderate-resolution of 10 m in the red, green, blue, and near-infrared bands (Laneve et al., 2021).

194 -The optical data collected from the ESA platform (Sentinel-2) is treated and plotted using QGIS software to generate true
195 color images (bands 2, 3, and 4 corresponding to RGB), in the present study. We skipped The present study skips the image of
196 3rd, Aug 2020 due to bad weather conditions, so that only the two images collected and mentioned in the table 2bis above were
197 used to validate the ground changes detected by InSAR.

198 4 Application to the case study and results

199 The case studies are located in two different sites and both areas of interest are located in Algeria. They have a hilly relief: the
200 first one is located northeast of Mila City (Graum) and the second is at the west part of Mila City (Kherba). To monitor the
201 AoIs, several available-images are processed and used with different orbits directions (Ascending and Descending total of 35
202 ascending and descending acquisitions, see Fig. 1), in order-to catch deformation from different angles along the sensor's LOS.
203 The InSAR technique is used in both areas, in order-to detect land deformation and landslides caused/triggered by the
204 earthquake.

205 The present study uses Sentinel 1 A and B datasets: The Sentinel 1 sensors have a wavelength of 5.546 cm (ESA) and are
206 right side looking with an incidence angle ranging approximately from 20° to 46° (ESA, 2012), which are suitable for change
207 detection and the monitoring of large areas. Furthermore, optical sensors data from Sentinel 2 are used in order to validate the
208 ground changes detected by InSAR.

The ~~four~~ adopted methods are applied for Mila case study ~~in order to~~:

- detect and measure the co-event surface displacements and landslides, caused by the earthquake (CCD and DInSAR)
- monitor their dynamic evolution in the first weeks and months, at the post-event period (CCD and LiCSAR data).
- analyze their possible initiation ahead of the earthquake by months and years, at the pre-event period (Time-series methods and LiCSAR data).
- corroborate the results by comparing several methods outputs, i.e. SAR (CCD, DInSAR, LiCSAR), aerial optical photo (Sentinel-2), and field surveys.

The quality of the SAR image is consistent with the topography slopes and area roughness. Actually, the AoI has rough topography, hills, and rivers (Fig. 2). Selecting either ascending or descending passes, relying on which will avoid some limitation of InSAR is an extremely essential action ~~able~~ to infer the deformation from various angles. Therefore, considering the regional topography and geology of the AoI is necessary to process InSAR and results interpreting.



Figure 4. 3D view of AoIs, Kherba AoI and Grarem using QGIS with DEM SRTM 1sec and ESRI basemap, a & b are Kherba AoI, c is the Grarem case area, the red polygon is the boundary of change detected by InSAR.

Differential InSAR (DInSAR) method is helpful to investigate co-seismic effects and detect ground changes ~~in the ground~~. The produced Interferograms and coherence images are projected to WGS84 reference, with a pixel size of 13.4 m. The unwrapped interferograms ~~below~~ present phase contribution of many noise resources (atmospheric), see Fig. 5. In general, strong earthquakes cause large-scale fringes patterns around the epicenter which is not the case in the event under study (a moderate earthquake). Processing DInSAR analysis may then lead to misinterpretation due to atmospheric contribution in differential phase interferograms (Fig. 5). In the study case, no regional deformation due to the earthquake is observed and there is no need to continue investigating the dam and the two bridges by simple DInSAR. However, to monitor the dam and bridges, it is highly recommended to use PS-InSAR for regional and local ground deformation detection (Hooper et al., 2004; Rapant et al., 2020; Sanabria et al., 2014).

~~this moderate earthquake has triggered small deformation and landslides in Grarem, Kherba, and Azeba, see Figs. 7, 10, and 20.~~

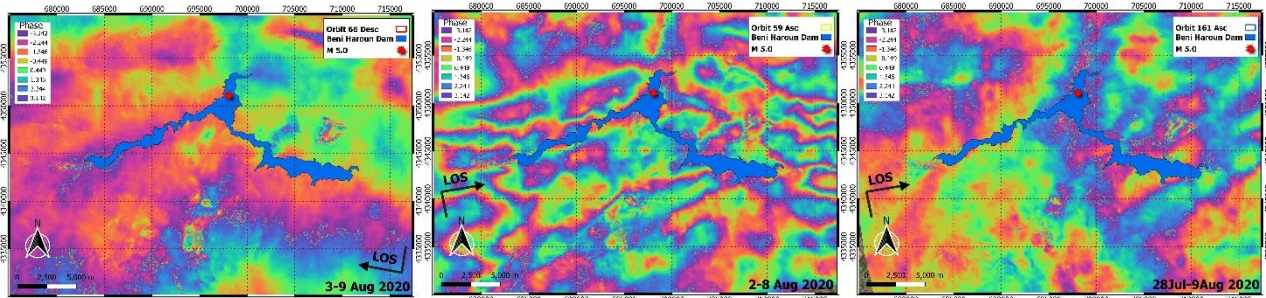
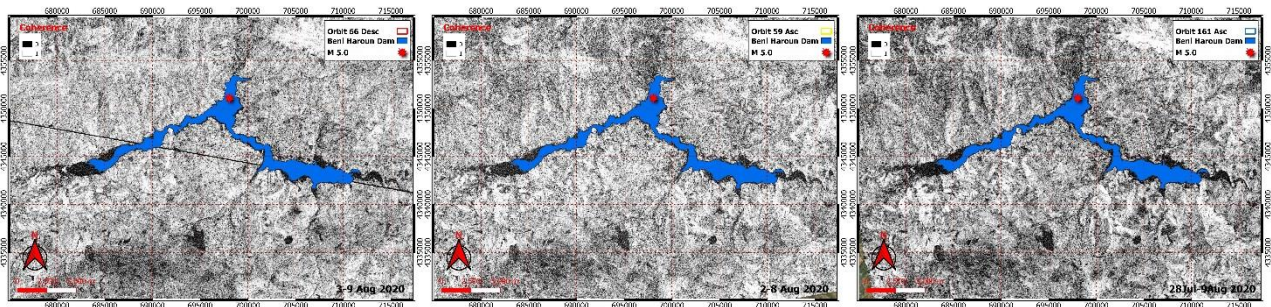


Figure 5. Wrapped Interferograms from Sentinel-1 for IFG-3+IFG-4, IFG-17 and IFG-22, The red star is the epicenter location (USGS).



237

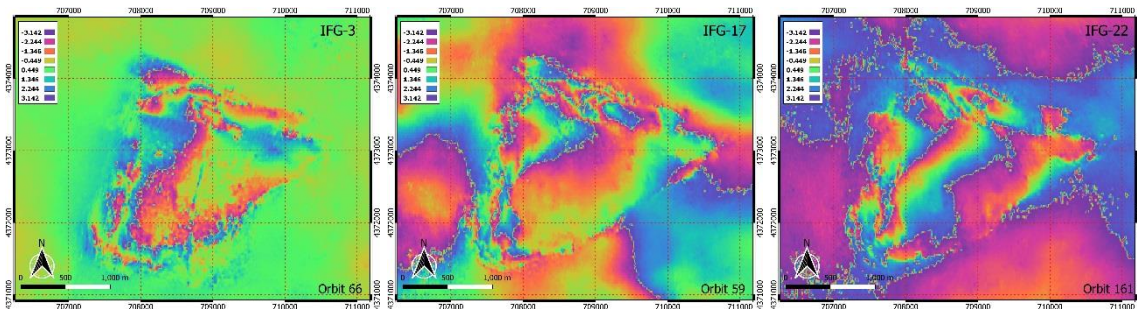
238 **Figure 6.** Mila Area, InSAR coherence maps for IFG-3+IFG-4, IFG-17 and IFG-22.

239 This moderate earthquake has triggered small deformation and landslides in Grarem, Kherba, and Azeba, see Figs. 7, 10,
 240 and 20.

241 The IFG-3 and IFG-4 are merged in one image due to the AoIs (Kherba and Grarem), which are located between-in two
 242 different image acquisitions in-of the descending orbit number 66. In order to monitor the dam and bridges, it is highly
 243 recommended to use PS InSAR for regional and local ground deformation detection.

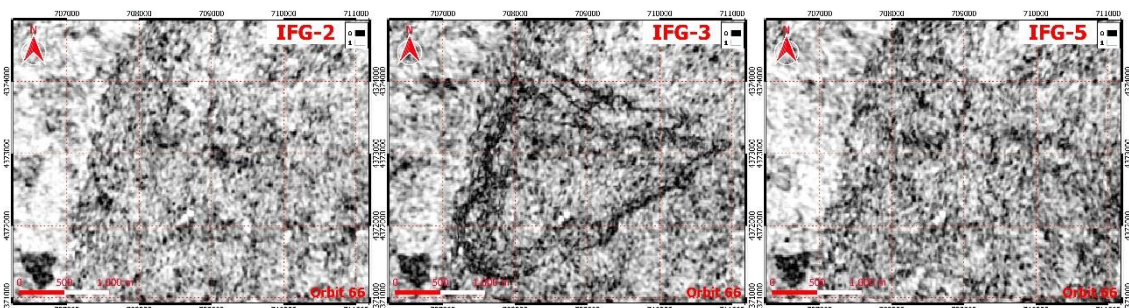
244 **4.1 Case of GRAREM**

245 The detection of deformation or changes between two InSAR images reveals a small change in the region of Grarem. This
 246 change is detected-observed as small fringes, each fringe corresponding to a displacement of a half-wavelength ($\lambda=5.546$ cm)
 247 in the LOS direction (Fig. 7). Usually, coherent change does not appear in coherence images as dark region, but in the study
 248 case, the outer borderline of the fringes region shows incoherence change which is clearly visible in coherence maps (Fig. 8).

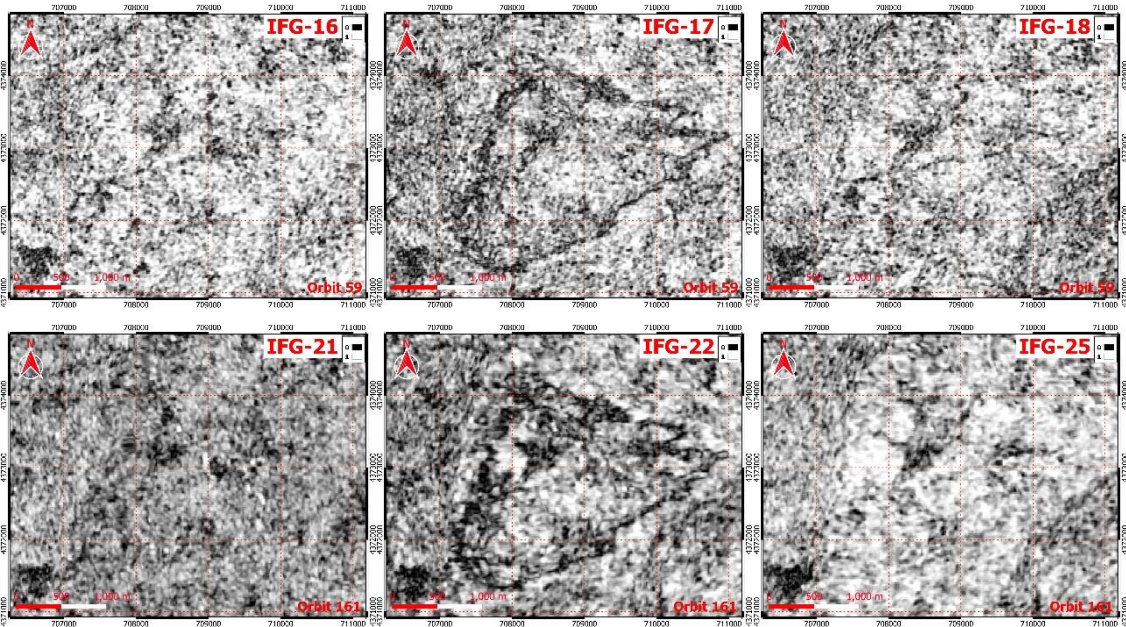


249 **Figure 7.** Detected fringes in Interferograms N° 3, 17, and 22, focused images on Grarem zone.

251 A time-time-series analysis needs then to be performed out to prove whether this contour was formed at the event occurrence
 252 date (August 7, 2020). The coherence maps of the co-event period present a dark polygon which-that is related to incoherent
 253 change or deformation. But inside the AoI, the results show a-some coherent changes which means that this area has deformed
 254 as a block up or down.



255



256

257

258

259

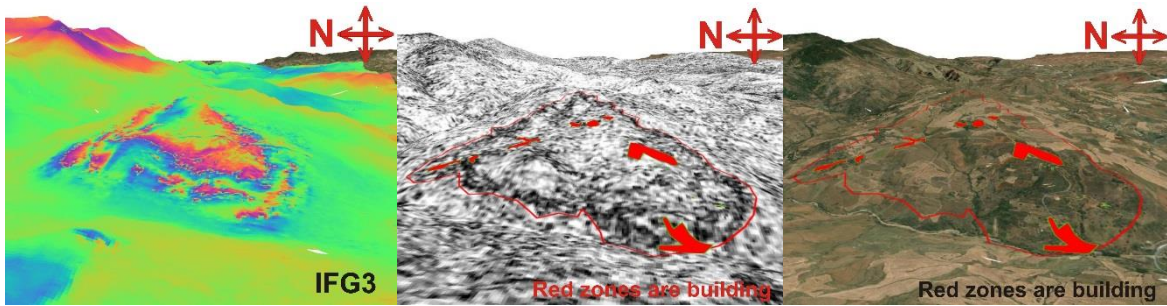
260

261

262

263

Figure 8. Coherence maps of Grarem AoI: the images represent pre-event (left), co-event (middle), and post-event (right) for each-orbits 66, 59, and 161. *Nota: –the co-event maps for the three orbits show the decay of coherence that is triggered by the earthquake.* According to phase and coherence maps, ~~The~~ affected area is approximately covers about 3.94 km² as estimated from phase and coherence maps, with an average runout distance of 2.6 km from the top to downhill of 2.6 km (Fig. 2 a distance from point 1 to point 2).



264

265

266

Figure 9. 3D view of Grarem Area, Images of IFG-3. Each fringe = wavelength/2 in LOS, and red zones represent existing building compounds (QGIS, ESRI basemap).

267

4.2 Case of Kherba

268

269

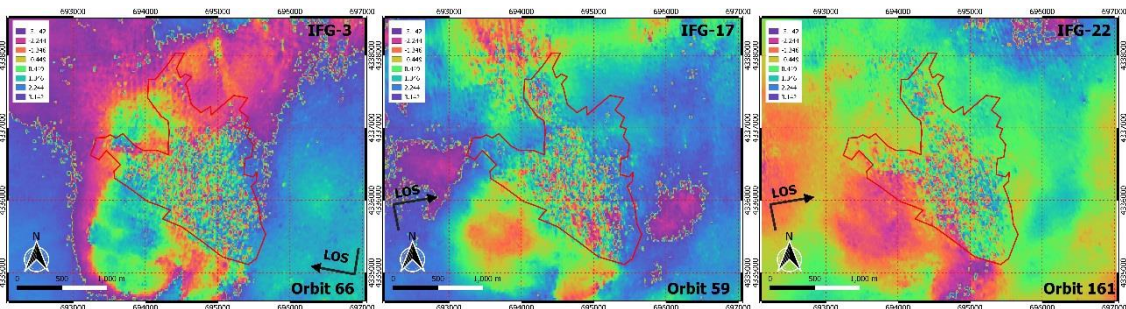
270

271

272

DInSAR ~~has abundantly demonstrated its reliability as a technique for monitoring slow movements~~ is expected to be more suitable for slow and gradual movements (Cascini et al., 2013; Wempen, 2020). In the present study, Kherba’s landslides exceed the capabilities of DInSAR since this method cannot measure the ~~changes-deformations~~ due to incoherent change at the first event. Phase images of the Region of Interest (RoI) show a clear decorrelation and consequently, the phase information is no longer convenient for analysis.

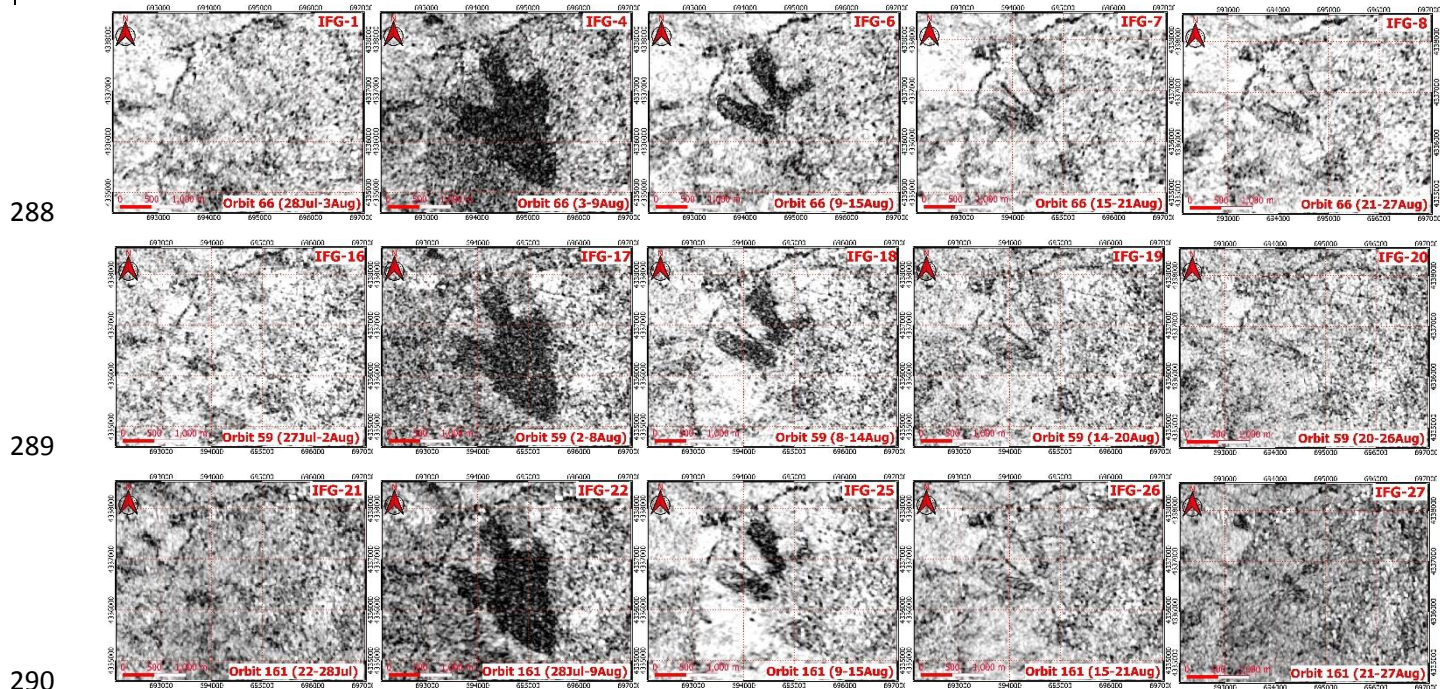
273



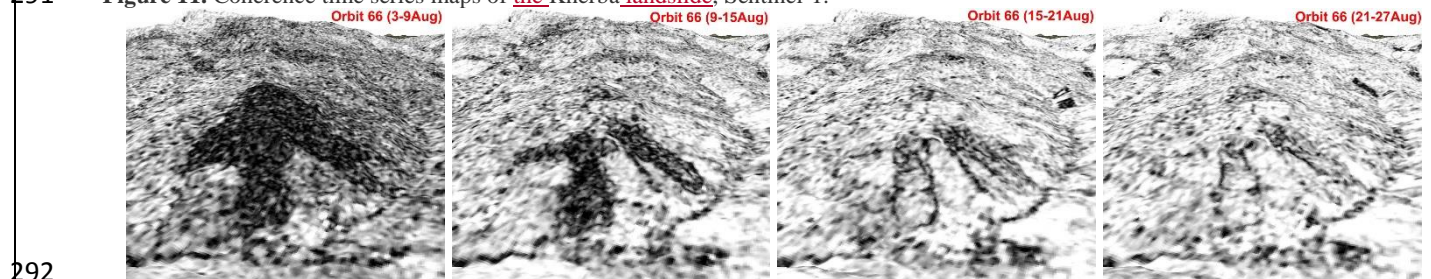
274 Figure 10. Kherba main event interferograms, biased pixels ~~in~~ inside the ~~RoI~~ red line correspond to incoherent changes.
 275 In such cases of incoherent changes in the scene, DInSAR is useless whereas we can serve to the Coherence Change Detection
 276 coherence change detection (CCD) method which is remains useful and suitable and able to monitor the event.

277 4.2.1 CCD Times series analyses

278 For the case study, the coherence maps (Figs. 11-13) show very low coherence in the Kherba area (~~RoI~~) and, indicating that
 279 some changes have occurred. ~~This may confirm whether the decrease of coherence values is due to the hazard or it is naturally~~
 280 ~~low.~~ The Coherence Change Detection (CCD) is useful when the change is incoherent in the scene, since CCD quantifies
 281 changes between two SAR images, and ~~is~~ is represented as a decay of coherence values (co-event maps). ~~This may confirm~~
 282 ~~whether the d~~ Decreases of in coherence values can be caused by a variety of factors such as earthquake, geotechnical landslides
 283 as well as including is due to the hazards or it is being naturally low (e.g., water, vegetation...). To distinguish between
 284 natural low coherence (e.g., water, vegetation...) and induced surface changes, a second coherence map (pre-event or post-
 285 event) is needed required in order to serve as a reference reference and to, which can be compared with the main pre-co-event
 286 images. It is preferable to mask out the rest of the non-changed area using with a ratio of pre-event by to co-event image ratio
 287 and filter values that are equal to or less than 1 (see Fig. 13).



291 Figure 11. Coherence time series maps of the Kherba landslide, Sentinel-1.

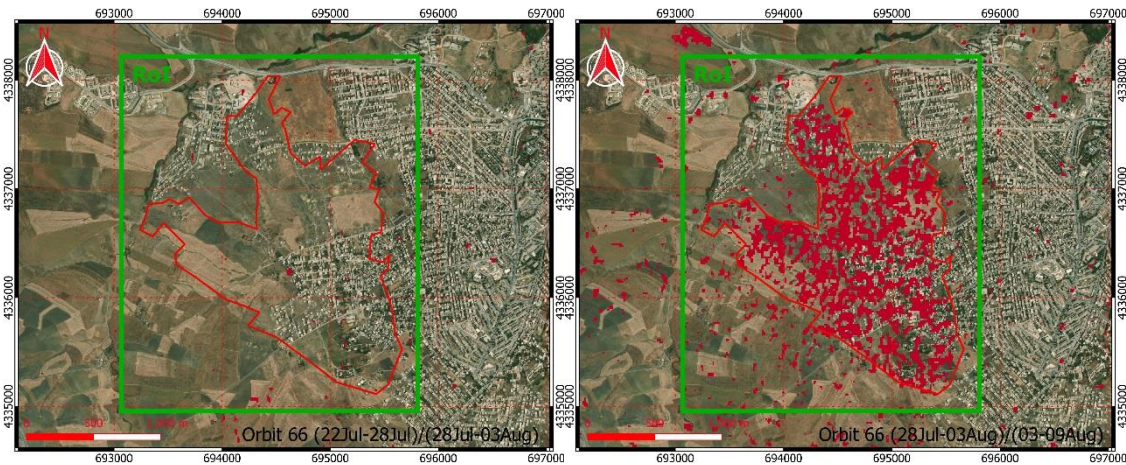


292 Figure 12. 3D view of Kherba City landslide, Sentinel-1 Coherence images of Orbit 66 with a 6-day temporal baseline, the dark areas are
 293 the landslide and deformations zones.

294 The CCD time-series analysis displays the changes in the AoI over time for the Kherba landslide. The dark region represents
 295 the main changes that occurred during the co-event period (earthquake date). The landslide shape is divided into two toes at
 296 the lower side of the Hill, as shown in Figs. 11 and 12.

298 During the first week following the earthquake, changes are detected in the lower side of the hill, and lasted until the late date
 299 of August 2020 (IFG-8 orbits 66, IFG-27 orbit 161, and IFG-20 for orbit 59). Afterwards, many other sources of noise were
 300 present in the AoI, which makes this technique less efficient (weather, human activities). Most of the processed images are 6
 301 days' intervals, except the orbit 161 in which the co-event image interferogram (IFG-24) was not good enough good (bad
 302 coherence) to compare with other pre-post-event images; it is then so it was replaced by the IFG-22. Figures 14 and 15
 303 illustrate how the image interferograms selection may change the interpretation of results.

304 To quantify the change, an RoI is represented in Fig. 13 (green rectangle) is selected for analysis, and the The plots in
 305 Figs. 14 and 15 show also the frequency distributions of coherence values within the RoI. Table 3 displays the calculated
 306 average coherence values of the RoI and the decreased percentage values inside the RoI of changes. For the 66 orbit's 66 pairs,
 307 the RoI average coherence starts by 0.66 during the pre-event period (IFG-2) and decreases to 0.51 during the co-event period
 308 (-3423%) (IFG-3). For orbit 59 pairs, it decreases by 2722% after an initial mean value of 0.77 (IFG-16) with and a mean value
 309 of 0.60 (IFG-17) after an initial mean value of 0.77 (IFG-16).



310
 311 **Figure 13.** Pre-event coherences ratio (left), co-event coherences ratio (right), Sentinel-1 Orbit 66. The green box indicates the scope of the
 312 RoI, red spots represent significant changes of coherence in the landslide region (QGIS, ESRI World Imagery basemap).

313 The last orbit 161 pairs make an exception due to an the initial bad coherence maps (IFG-23 and 24), as shown in Fig. 15,
 314 where the dotted green line has low coherence compared to the co-event coherence map (red dotted line). So, the orbit 161
 315 acquisition of the 3rd August must be skipped and not used for the analysis and the interpretation. And it was replaced by the
 316 previous acquisition of on July- 28th. see Fig. 14.e. However, the previous pair (IFG-21 and IFG-22) gave had a value of 0.57
 317 (IFG-21) which that decreased to 0.52 (IFG-22), representing a 9 percent i.e. 11% of change.

318 **Table 3.** Mean coherence change values inside the ROI.

Orbit	Pre-event coherence mean	Co-event coherence mean	Post-event coherence mean	Pre-event Change	Post-event Change
66	28Jul_03Aug 0.66	03_09Aug 0.51	09_15Aug 0.63	-3423%	+24%
59	27Jul_02Aug 0.77	02_08Aug 0.60	08_14Aug 0.69	-2722%	+15%
161	22Jul_28Jul 0.57	28Jul_09Aug 0.52	09Aug_15Aug 0.71	-119%	+37%

319 The lines in Figure 14 indicate the frequency distributions of coherence time series maps. The green line in Fig.14.a represents
 320 the pre-event coherence distribution, while the red line represents the post-event coherence distribution, which clearly shows
 321 a decay of the mean coherence after the main event (dates and values are presented in the legend).

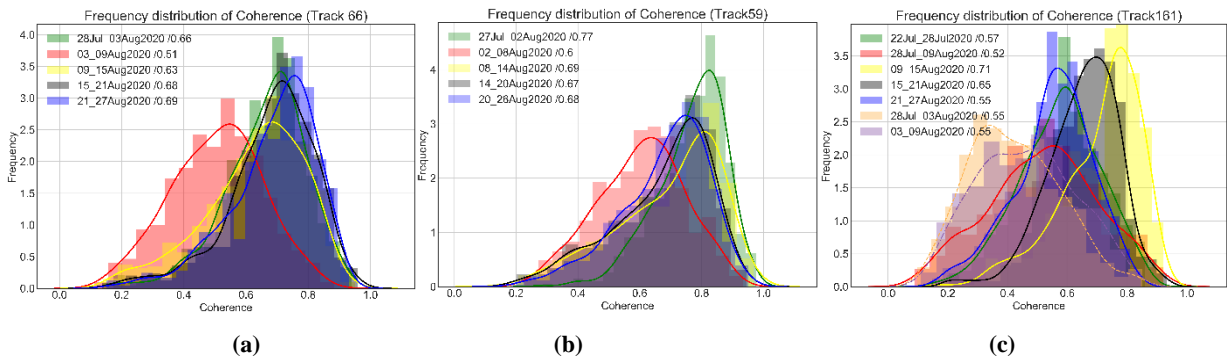


Figure 14. Frequency distributions of coherence values within RoI for all coherence time series images.

Figure 15 illustrates why ~~we chose the interferogram of the 22-28July (green line) is chosen as the pre-event (initial) even though there is another IFG of (28July-3Aug green dotted line) with i.e. only four days before the main event (7 August 2020).~~

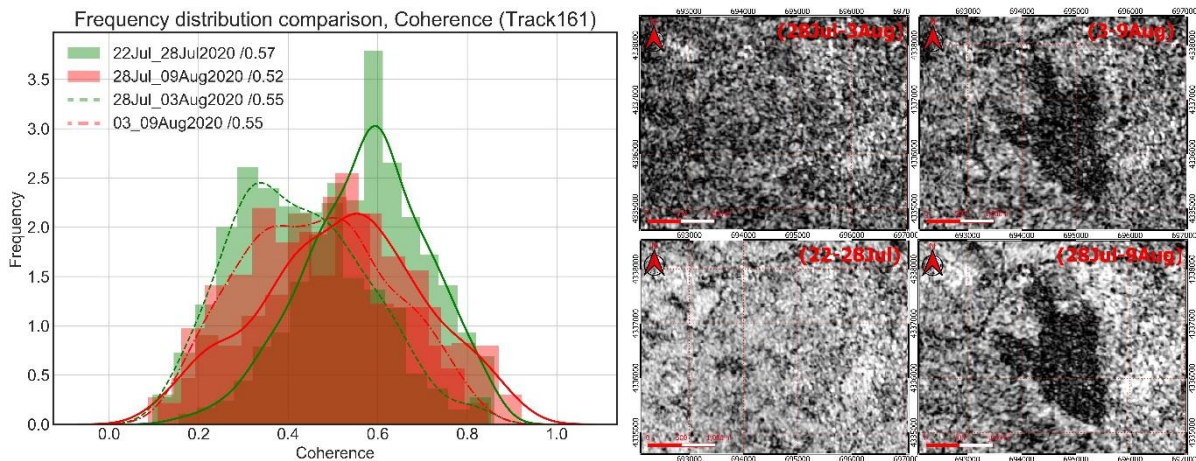


Figure 15. Effect of bad coherence ~~shift~~: the cause is the acquisition of 3rd August start at (17:28:15, orbit 161) under bad weather conditions in the acquisition time according to precipitation site (WWO) (rainfall in that daytime), compared to the acquisition of the same day but not the same time (05:37:58 for orbit 66).

The surface area derived from the coherence images covers 2.1 km², ~~derived from the coherence images~~, and the shape ends by two toes. The runout distance is 2.4 km for the right toe and 2.15 km for the left one. The CCD method has the potential to differentiate between the areas impacted by induced changes and those affected by other sources of noise. The ratio operation is useful in canceling out other noise factors and improvinge the detection of changes in the region.

4.2.2 Optical detection

To validate the SAR methods results, two images from Sentinel-2 are downloaded and treated using QGIS software, the dates of the images being dated 2020-07-30 (a week before the main shock), and 2020-08-09 (two days after the main shock); and the optical data is treated using QGIS.

- The optical passive-detection shows that an important ground surface-displacement affected the ground of in the Kherba neighborhood, over an area of 1.32 km². The landslide shape of deformation has only one toe at the lower part of the hill (blue line Fig. 16.b) compared to the CCD method results.

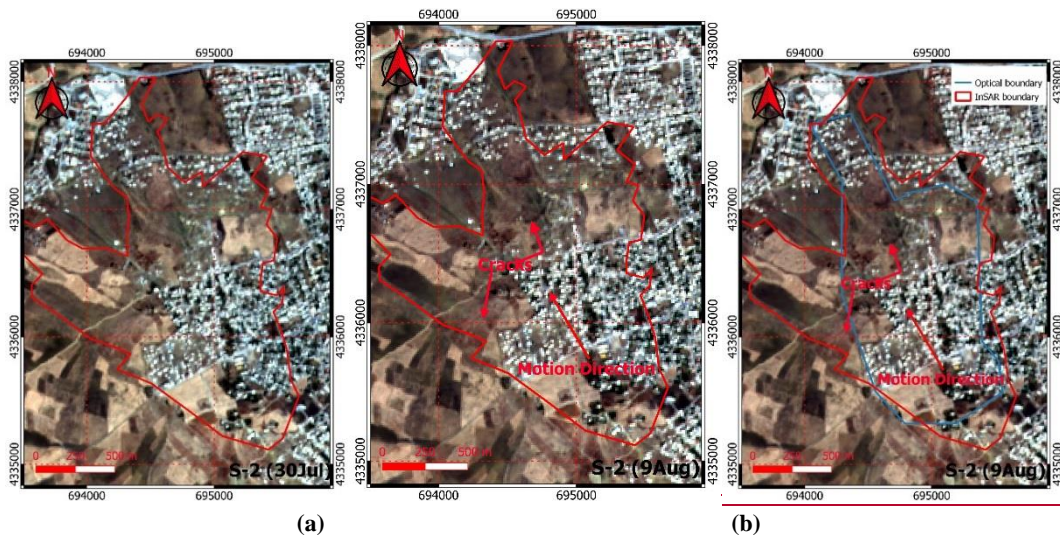


Figure 16. Sentinel-2 Optic Images: (a)- dated 30-Jul 2020, (b)- dated 09-Aug 2020.

The optical images were unable to detect the disorders ground deformations and displacements in Grarem in which there was no apparent landslide although there were a lot of ruptures and cracks. However, a field inspection has confirmed the results of the CCD and DInSAR analysis in terms of pattern and limits of the zone affected by the deformation (surface rupture).

4.3 LiCSBAS analyses

LiCSBAS is an open source program for InSAR time series analysis based on LiCSAR data. The LiCSAR system automatically processes Sentinel-1 InSAR datasets (Lazecký et al., 2020b), to generate wrapped, unwrapped interferograms and coherence maps (Lazecký et al., 2020b), with a final product resolution of ~26.5 m (Lazecký et al., 2020a). LiCSBAS exploits the data of LiCSAR in order to generate maps of displacement mean velocity and deformation time series plots (Morishita, 2021).

Displacement time series and velocities analysis of the region is performed out using LiCSBAS that exploits the data of the LiCSAR system (Morishita, 2021). It allows identifying whether unstable conditions pre-existed or are still undergoing. The study started from the 5th of April to the 26th of September 2020, for the orbit 66 and from 26 April 2015 to 26 September 2020 for the orbit N° 161.

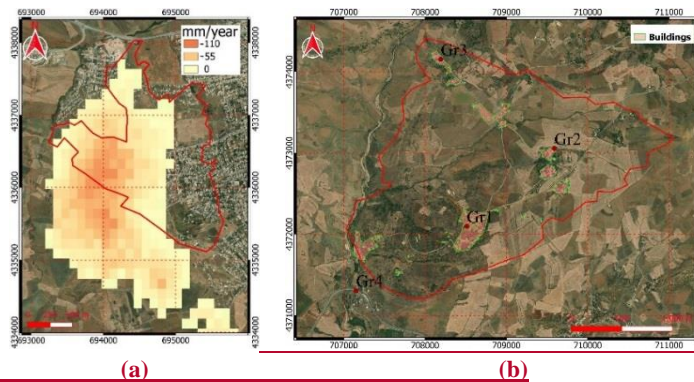
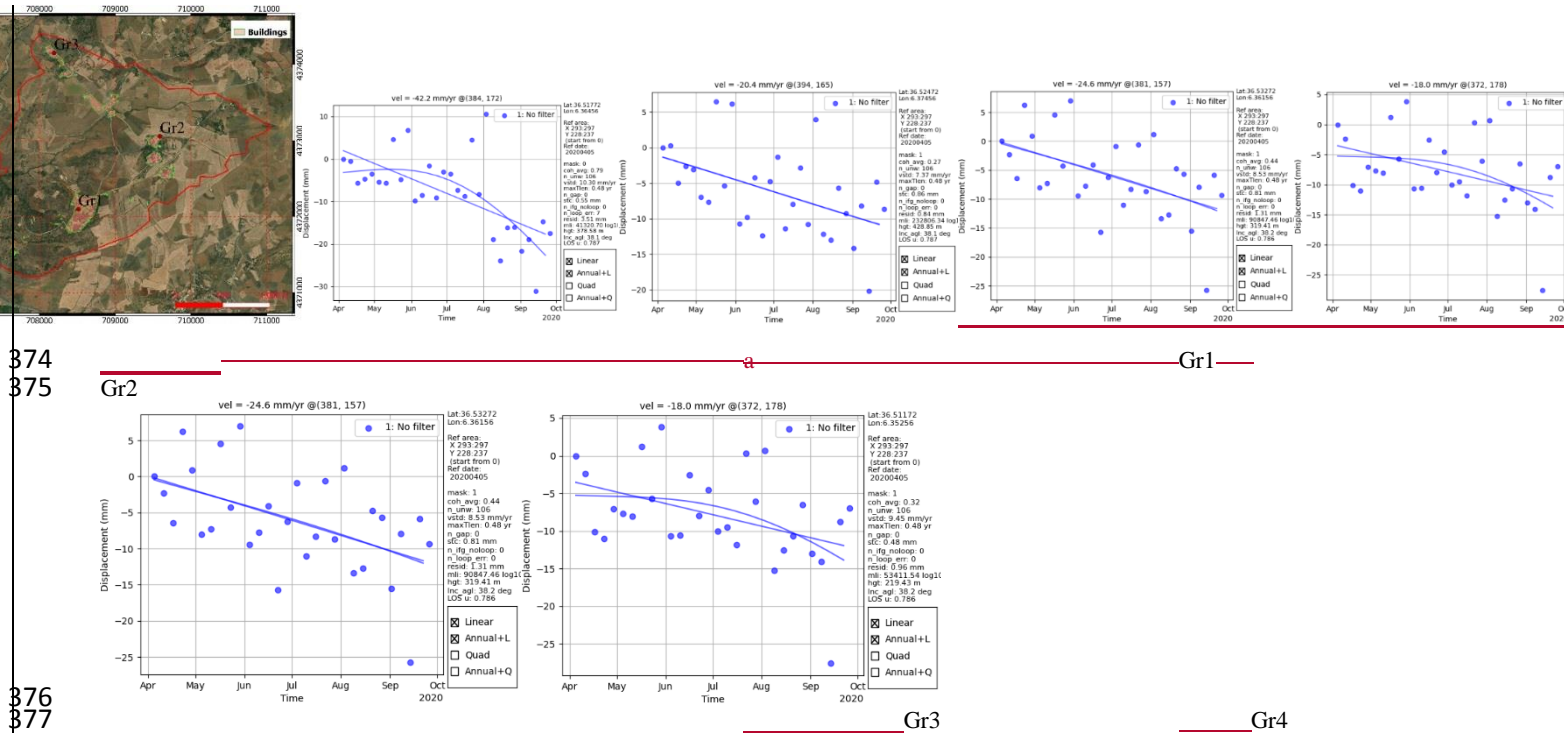


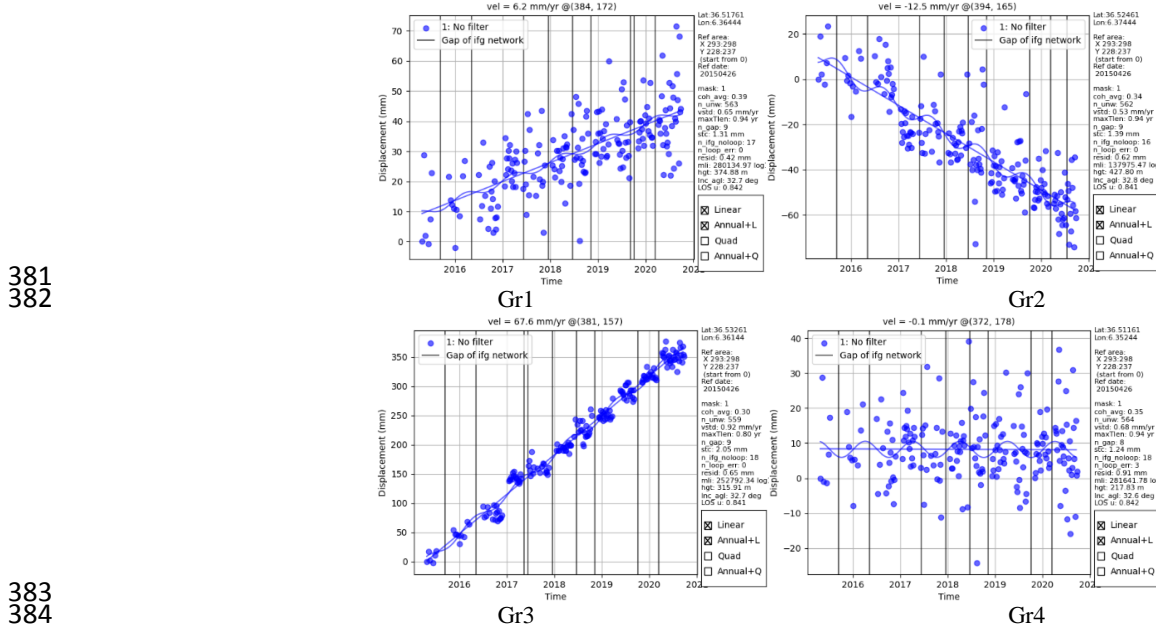
Figure 17. (a) Line of sight (LOS) displacement velocity map, the red line is landslide area (066D_05394_131311), (b) Grarem case selected points for time-series analysis. (QGIS, ESRI basemap).

The time-series analysis detected subsidence at of the west part of Kherba. This region is on the other hillside of Kherba Hill, and both sides have a significant slope. A site investigation did not find any drilled wells. One may assume that this subsidence is not caused due to any by the pumping of groundwater. Therefore, another possible explanation is probably related to the large mass movement of the main landslide hillside (red polygon), causing the opposite side of the hill to move down (subsidence). The displacement velocity in Kherba is about 110 mm/year, Fig. 17.

370 For the Grarem case, the velocity map looks stable between the same dates (April 5 to September 26, 2021+2020). The
 371 change occurred rapidly and is removed by the filters. For illustrative purposes, the displacement time series of some points
 372 are illustrated in Figs. 18 and 19.



376
 377
 378 **Figure 18.** Displacement time series (orbit 66, Grarem case), corresponding to the points in image (a17.b), the displacement is relative to
 379 the a reference point, (a) Grarem region, the plots presents a great dispersion of data points which is related to many noise resources (weather,
 380 man-made, etc.), and short period of analysis. (QGIS, ESRI basemap).



381
 382
 383
 384
 385 **Figure 19.** Displacement time series (orbit 161), corresponding to the points in Fig. 187. ab, displacement is relative to the reference point
 386 The plots show less dispersion of data points (linear) compared to short analysis, the long period analysis (5 years) is useful to eliminate
 387 other sources of noise.-

388 During the LiCSBAS processing, a primary stable reference point is selected at (36.455885° N, 6.276909° E). This method
 389 proves to be efficient for large-scale deformation monitoring and slow coherent changes, long time series analysis is useful in
 390 reducing other noise factors.

391 **4.4 Discussion**

392 InSAR monitoring proves its ability to detect land changes. First, landslides and land deformation can be detected remotely by
393 InSAR. Furthermore, optical images could detect only one case (Kherba). The theoretical results were validated by site visiting
394 and investigation, i.e.:

- 395 - Compared to results obtained from optical for the Kherba landslide, InSAR is more precise for detecting small
396 deformation (2 toes in CCD maps). Besides, the ~~other optical techniques way analysis~~ did not detect the full deformed
397 changing area in the region (only one toe).
- 398 - Large-scale ~~landslides of this magnitude~~ exceed DInSAR's ~~the capabilities of DInSAR, and their~~ which induce an
399 extreme loss of coherence. The -co-event ~~interferograms of co-events~~ are strongly decorrelated. Therefore, the phase
400 information is no longer usable and one cannot measure the displacement of incoherent ground changes (Landslide).
- 401 - Land deformation in Grarem first detected by DInSAR, was confirmed by a site visit, during which small cracks were
402 visible on the ground (incoherent boundary region). Due to incoherent boundaries and because the displacement is
403 probably larger than what can be measured by one interferogram fringe cycle (depending on the wavelength, 5 cm for
404 Sentinel-1), the deformation measurements in this case are not reliable and accurate.
- 405 - Another landslide detected by InSAR in the Azeba region (6 km east of Mila) was visited too: the area covers 0.42 km²
406 and the site investigation (~~Fig. 20~~) confirms the landslide (Fig. 20).
- 407 - Analysis with LiCSBAS revealed new hillside deformation (subsidence) which is probably a consequence of the mass
408 that moved in the main landslide hillside. Displacements time series, ~~in of the~~ Grarem region at some points, show
409 deformation along LOS with velocities ranging from 6 mm/year to 67 mm/year. This method is preferable in ~~the~~ large-
410 scale area and large long-period analysis.



411
412 **Figure 20.** Landslide occurred in Azeba region (2 km North) detected by InSAR: (a) & (b)- visible ground cracks, (c)- coherence map of
413 Azeba zone delimited by the cracks.
414

415 5 Conclusions and Recommendations

416 In this paper, active and passive space-based satellite data are used to monitor and study the impact of natural hazards
417 (earthquakes and landslides) on struck areas. The C-band Sentinel-1 SAR datasets (active sensing) and optical images of
418 Sentinel-2 data (10 m spatial resolution) were used in this study to investigate the area, the passive images were used only to
419 validate the active sensing results. For the InSAR processing, the use of DInSAR, CCD methods, and the LiCSBAS tools has
420 have been able to generate a detailed time series analysis of ground changes.

421 InSAR techniques have proved their efficacy efficiency can to extract useful geodetic information, such as the ground
422 movement and track surface deformation over large areas with centimetric accuracy in coherent change cases. The present
423 research study has demonstrated that the InSAR processing is adapted to study earthquake and landslides zones. As a result,
424 three primary land failures were detected over the study area using InSAR.

425 DInSAR is poorly suited to track and detected landslides. It is represented as a pixel decorrelation in phase interferograms and
426 high decay in coherence values. CCD is further suitable to map earthquake-induced landslides that may remain undetected
427 using coherent methods (DInSAR). The estimation of their horizontal/vertical displacements is a challenge to be inferred.

428 The Grarem deformation looks ~~like~~as a landslide that has just been initiated, but might extend under an upcoming triggering
429 event. Actually, the failure plane rim is presented as a dark line in the coherence map or as the ~~fringe~~ circumference ~~of the~~
430 ~~fringe~~-in phase maps (estimated area 3.94 sq. km). This impending land failure needs therefore a thorough and real-time
431 monitoring ~~by the and adequate geotechnical studies~~. PS-InSAR ~~method, which~~ can ~~serve as an provide~~ efficient and low-cost
432 monitoring method able to obtain millimeter-level precision displacement measurements over selected points in the area (~~Jia~~
433 ~~et al., 2019~~), (~~Jia et al., 2019~~), and ~~adequate geotechnical studies~~.

434 It is worth ~~to increase~~increasing awareness of possible future geotechnical threats in a timely manner, through on-site
435 monitoring using GPS, crack meters, and by placing inclinometers in the Grarem area, in order to develop a model of the slope
436 stability.

437 **Acknowledgments:** In this work, we used SNAP and QGIS to analyze and plot maps. ~~ESA, Copernicus, and COMET for~~
438 ~~providing Sentinel data~~. The authors are grateful to European Space Agency (ESA) for providing freely the data through
439 Copernicus Program ~~and COMET~~.

440 **Conflicts of Interest:** The authors declare no conflict of interest.

441 References

- 442 ASF DAAC: Alaska Satellite Facility, [online] Available from: <https://search.asf.alaska.edu/#/> (Accessed 26 June 2021), n.d.
- 443 Bakon, M., Perissin, D., Lazecky, M. and Papco, J.: Infrastructure Non-linear Deformation Monitoring Via Satellite Radar
444 Interferometry, *Procedia Technol.*, 16, 294–300, doi:10.1016/j.protcy.2014.10.095, 2014.
- 445 Braun, A.: Radar satellite imagery for humanitarian response: Bridging the gap between technology and application, , 225
446 [online] Available from: https://publikationen.uni-tuebingen.de/xmlui/bitstream/handle/10900/91317/Braun_2019_Radar_satellite_imagery_for_humanitarian_response_UB.pdf?sequence=1, 2019.
- 447 Canaslan Çomut, F., Gürboğa, Ş. and Smail, T.: Estimation of co-seismic land deformation due to Mw 7.3 2017 earthquake
448 in Iran (12 November 2017) using Sentinel-1 DInSAR, *Bull. Miner. Res. Explor.*, 162(August), 11–30,
449 doi:10.19111/bulletinofmre.604026, 2020.
- 450 Cascini, L., Peduto, D., Pisciotta, G., Arena, L., Ferlisi, S. and Fornaro, G.: The combination of DInSAR and facility damage
451 data for the updating of slow-moving landslide inventory maps at medium scale, *Nat. Hazards Earth Syst. Sci.*, 13(6), 1527–
452 1549, doi:10.5194/nhess-13-1527-2013, 2013.
- 453 Congedo, L.: Semi-Automatic Classification Plugin: A Python tool for the download and processing of remote sensing
454 images in QGIS, *J. Open Source Softw.*, 6(64), 3172, doi:10.21105/joss.03172, 2021.
- 455 Del, M. and Idrogeologico, R.: Landslides forecasting analysis by displacement time series, *Geology*, 2011(January), 19–23,
456 2012.
- 457 ESA: ESA’s radar observatory mission for GMES operational services. [online] Available from:
458 https://sentinel.esa.int/documents/247904/349449/S1_SP-1322_1.pdf, 2012.
- 459 ESA: Resolution and Swath - Sentinel-1 - Missions - Sentinel Online - Sentinel, [online] Available from:
460 <https://sentinel.esa.int/web/sentinel/missions/sentinel-1/instrument-payload/resolution-swath> (Accessed 26 June 2021a), n.d.
- 461 ESA: SAR Instrument - Sentinel-1 SAR Technical Guide - Sentinel Online - Sentinel, [online] Available from:
462 <https://sentinels.copernicus.eu/web/sentinel/technical-guides/sentinel-1-sar/sar-instrument> (Accessed 26 June 2021b), n.d.
- 463 Frizon de Lamotte, D., de Lamotte, D. F., Bezar, B., Saint, Bracène, R. and Mercier, E.: The two main steps of the Atlas
464 building and geodynamics of the western Mediterranean, *Tectonics*, 19(4), 740–761 [online] Available from:
465 https://www.academia.edu/29649745/The_two_main_steps_of_the_Atlas_building_and_geodynamics_of_the_western_Mediterranean
466 (Accessed 6 January 2022), 2000.

468 Galve, J. P., Castañeda, C. and Gutiérrez, F.: Railway deformation detected by DInSAR over active sinkholes in the Ebro
469 Valley evaporite karst, Spain, *Nat. Hazards Earth Syst. Sci.*, 15(11), 2439–2448, doi:10.5194/nhess-15-2439-2015, 2015.

470 Goudarzi, M. a: Detection and measurement of land deformations caused by seismic events using InSAR, Sub-pixel
471 correlation, and Inversion techniques, , (January), 127, 2010.

472 Herrera, G., Fernández, J. A., Tomás, R., Cooksley, G. and Mulas, J.: Advanced interpretation of subsidence in Murcia (SE
473 Spain) using A-DInSAR data - Modelling and validation, *Nat. Hazards Earth Syst. Sci.*, 9(3), 647–661, doi:10.5194/nhess-9-
474 647-2009, 2009.

475 Hooper, A., Zebker, H., Segall, P. and Kampes, B.: A new method for measuring deformation on volcanoes and other natural
476 terrains using InSAR persistent scatterers, *Geophys. Res. Lett.*, 31(23), 1–5, doi:10.1029/2004GL021737, 2004.

477 Jacquemart, M. and Tiampo, K.: Leveraging time series analysis of radar coherence and normalized difference vegetation
478 index ratios to characterize pre-failure activity of the Mud Creek landslide, California, *Nat. Hazards Earth Syst. Sci.*, 21(2),
479 629–642, doi:10.5194/nhess-21-629-2021, 2021.

480 Jia, H., Zhang, H., Liu, L. and Liu, G.: Landslide deformation monitoring by adaptive distributed scatterer interferometric
481 synthetic aperture radar, *Remote Sens.*, 11(19), 1–18, doi:10.3390/rs11192273, 2019.

482 Jung, J. and Yun, S. H.: Evaluation of coherent and incoherent landslide detection methods based on synthetic aperture radar
483 for rapid response: A case study for the 2018 Hokkaido landslides, *Remote Sens.*, 12(2), 1–26, doi:10.3390/rs12020265,
484 2020.

485 Kim, J. W.: Applications of Synthetic Aperture Radar (SAR)/ SAR Interferometry (InSAR) for Monitoring of Wetland
486 Water Level and Land Subsidence, *Ohio State Univ.*, (503), 1–111, 2013.

487 Laneve, G., Bruno, M., Mukherjee, A., Messineo, V., Giuseppetti, R., De Pace, R., Magurano, F. and Ugo, E. D. ’: Remote
488 Sensing Detection of Algal Blooms in a Lake Impacted by Petroleum Hydrocarbons, *Remote Sens.* 2022, Vol. 14, Page 121,
489 14(1), 121, doi:10.3390/RS14010121, 2021.

490 Lazecký, M., Hatton, E., González, P. J., Hlaváčová, I., Jiráňková, E., Dvořák, F., Šustr, Z. and Martinovič, J.:
491 Displacements monitoring over Czechia by IT4S1 system for automatised interferometric measurements using Sentinel-1
492 data, *Remote Sens.*, 12(18), 1–21, doi:10.3390/RS12182960, 2020a.

493 Lazecký, M., Spaans, K., González, P. J., Maghsoudi, Y., Morishita, Y., Albino, F., Elliott, J., Greenall, N., Hatton, E.,
494 Hooper, A., Juncu, D., McDougall, A., Walters, R. J., Watson, C. S., Weiss, J. R. and Wright, T. J.: LiCSAR: An automatic
495 InSAR tool for measuring and monitoring tectonic and volcanic activity, *Remote Sens.*, 12(15), doi:10.3390/RS12152430,
496 2020b.

497 LNHC: Laboratoire National de l’Habitat et de la Construction, LNHC [online] Available from: <http://lnhc-dz.com/>
498 (Accessed 26 June 2021), n.d.

499 Meng, Q., Confuorto, P., Peng, Y., Raspini, F., Bianchini, S., Han, S., Liu, H. and Casagli, N.: Regional recognition and
500 classification of active loess landslides using two-dimensional deformation derived from sentinel-1 interferometric radar
501 data, *Remote Sens.*, 12(10), doi:10.3390/rs12101541, 2020.

502 Merghadi, A., Abderrahmane, B. and Tien Bui, D.: Landslide susceptibility assessment at Mila basin (Algeria): A
503 comparative assessment of prediction capability of advanced machine learning methods, *ISPRS Int. J. Geo-Information*,
504 7(7), doi:10.3390/ijgi7070268, 2018.

505 Moretto, S., Bozzano, F. and Mazzanti, P.: The role of satellite insar for landslide forecasting: Limitations and openings,
506 *Remote Sens.*, 13(18), 1–31, doi:10.3390/rs13183735, 2021.

507 Morishita, Y.: Nationwide urban ground deformation monitoring in Japan using Sentinel-1 LiCSAR products and LiCSBAS,
508 *Prog. Earth Planet. Sci.*, 8(1), doi:10.1186/s40645-020-00402-7, 2021.

509 Mouloud, H. and Badreddine, S.: Probabilistic seismic hazard assessment in the Constantine region, Northeast of Algeria,
510 *Arab. J. Geosci.*, 10(6), doi:10.1007/s12517-017-2876-5, 2017.

511 Netzband, M., Stefanov, W. L. and Redman, C.: Applied remote sensing for urban planning, governance and sustainability.,
512 2007.

513 Pawluszek-Filipiak, K. and Borkowski, A.: Integration of DInSAR and SBAS techniques to determine mining-related
514 deformations using Sentinel-1 data: The case study of rydułtowy mine in Poland, *Remote Sens.*, 12(2),
515 doi:10.3390/rs12020242, 2020.

516 Peláez Montilla, J. A., Hamdache, M. and Casado, C. L.: Seismic hazard in Northern Algeria using spatially smoothed
517 seismicity. Results for peak ground acceleration, *Tectonophysics*, 372(1–2), 105–119, doi:10.1016/S0040-1951(03)00234-8,
518 2003.

519 Rapant, P., Struhár, J. and Lazecký, M.: Radar interferometry as a comprehensive tool for monitoring the fault activity in the
520 vicinity of underground gas storage facilities, *Remote Sens.*, 12(2), doi:10.3390/rs12020271, 2020.

521 Roque, D., Perissin, D., Falcão, A. P., Fonseca, A. M. and Maria, J.: Dams regional safety warning using time-series insar
522 techniques, *Second Internatinal Dam World Conf.*, 21–24, 2015.

523 Sanabria, M. P., Guardiola-Albert, C., Tomás, R., Herrera, G., Prieto, A., Sánchez, H. and Tessitore, S.: Subsidence activity
524 maps derived from DInSAR data: Orihuela case study, *Nat. Hazards Earth Syst. Sci.*, 14(5), 1341–1360, doi:10.5194/nhess-
525 14-1341-2014, 2014.

526 Tampuu, T., Praks, J., Uiboupin, R. and Kull, A.: Long term interferometric temporal coherence and DInSAR phase in
527 Northern Peatlands, *Remote Sens.*, 12(10), 7–9, doi:10.3390/rs12101566, 2020.

528 Tzouvaras, M., Danezis, C. and Hadjimitsis, D. G.: Small scale landslide detection using Sentinel-1 interferometric SAR
529 coherence, *Remote Sens.*, 12(10), doi:10.3390/rs12101560, 2020.

530 USGS: M 5.0 - 3 km NNE of Sidi Mérouane, Algeria, [online] Available from:
531 <https://earthquake.usgs.gov/earthquakes/eventpage/us6000bag6/executive> (Accessed 26 June 2021a), n.d.

532 USGS: USGS Earthquake Hazards Program, [online] Available from: <https://earthquake.usgs.gov/> (Accessed 26 June
533 2021b), n.d.

534 Wang, Z., Li, Z. and Mills, J.: A new approach to selecting coherent pixels for ground-based SAR deformation monitoring,
535 *ISPRS J. Photogramm. Remote Sens.*, 144, 412–422, doi:10.1016/j.isprsjprs.2018.08.008, 2018.

536 Wempen, J. M.: International Journal of Mining Science and Technology Application of DInSAR for short period
537 monitoring of initial subsidence due to longwall mining in the mountain west United States, *Int. J. Min. Sci. Technol.*, 30(1),
538 33–37, doi:10.1016/j.ijmst.2019.12.011, 2020.

539 WWO: Mila, Mila, Algeria Historical Weather Almanac, [online] Available from:
540 <https://www.worldweatheronline.com/mila-weather-history/mila/dz.aspx> / (Accessed 26 June 2021), n.d.

541